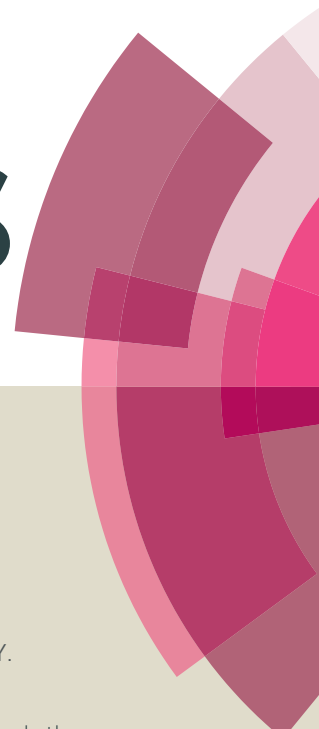


RSC Advances



This article can be cited before page numbers have been issued, to do this please use: A. Cao, G. Liu, Y. Yue, L. Zhang and Y. Liu, *RSC Adv.*, 2015, DOI: 10.1039/C5RA05190H.



This is an *Accepted Manuscript*, which has been through the Royal Society of Chemistry peer review process and has been accepted for publication.

Accepted Manuscripts are published online shortly after acceptance, before technical editing, formatting and proof reading. Using this free service, authors can make their results available to the community, in citable form, before we publish the edited article. This *Accepted Manuscript* will be replaced by the edited, formatted and paginated article as soon as this is available.

You can find more information about *Accepted Manuscripts* in the [Information for Authors](#).

Please note that technical editing may introduce minor changes to the text and/or graphics, which may alter content. The journal's standard [Terms & Conditions](#) and the [Ethical guidelines](#) still apply. In no event shall the Royal Society of Chemistry be held responsible for any errors or omissions in this *Accepted Manuscript* or any consequences arising from the use of any information it contains.



Nanoparticles of Cu-Co alloy derived from layered double hydroxides and their catalytic performance for higher alcohols synthesis from syngas

Ang Cao^{a, b}, Guilong Liu^{a, b}, Yizhi Yue^{a, b}, Lihong Zhang^{a, b}, Yuan Liu^{* a, b}

Received 00th January 20xx,
Accepted 00th January 20xx

DOI: 10.1039/x0xx00000x

www.rsc.org/

A series of layered double hydroxides (LDHs) with different Cu/Co ratio were prepared according to the co-precipitation method and used as catalyst precursors for higher alcohols synthesis. The prepared samples were characterized by XRD, TPR, SEM, TEM and BET techniques. After calcination, LDHs were transformed into a mixture of CuO, Co₃O₄, CuCo₂O₄ and alumina, and these oxides were mixed uniformly with size in several nanometers. For the sample with ratio of Cu/Co = 1/2, copper and cobalt species are mainly in CuCo₂O₄ phase. In the reduction process, the superior mixed copper and cobalt species in nanoscale were reduced to Cu-Co alloy, which was confirmed by XRD and TEM results. The prepared bimetallic catalysts showed high activity, good stability and much high selectivity to C₂₊ alcohols. Over the best catalyst, CO conversion of 51.8%, selectivity to alcohols of 45.8% and 94.3 wt. % of C₂-OH in the total alcohols were obtained at 250°C, 3MPa and GHSV of 3900 mL (g_{cat} h)⁻¹.

1. Introduction

With the dwindling of petroleum resource and the increasing consumption for energy, developing alternative fuels for the sustainable world economics are urgently needed.^{1, 2} Higher alcohols synthesis (HAS) via syngas from coal, natural gas or renewable biomass has attracted a considerable amount of attention due to the potential application of higher alcohols as motor fuels, gasoline blends additives and other intermediates for chemical feed stocks³⁻⁵.

However, the existing technologies for HAS are still in the laboratory stage, one of the critical problem is that the selectivity to C₂₊ alcohols is too low. Over most of the catalysts reported, methanol is the main product instead of higher alcohols. The price of each C₂₊ alcohols, including ethanol, propyl alcohol and butyl alcohol, is more than twice of that of methanol, and production of methanol is

industrialized for tens of years with methanol selectivity close to 100%. Therefore, only the selectivity to C₂₊ alcohols is high enough, excluding separation cost, HAS may be of value for industrialization.

Catalysts for HAS from syngas can be categorized to four types, including the modified methanol catalysts, Rh-based catalysts, Mo-based catalysts and modified Fisher-Tropsch catalysts. Modified methanol synthesis catalysts produce mainly methanol⁶. Rh-based catalysts possess a comparatively high selectivity to ethanol and good activity^{7, 8}, while the price of Rh is too high. Mo-based catalysts exhibit excellent sulfur resistance, however, they must be operated at high pressures and temperatures, and usually a long activity induction period before the reaction is required^{9, 10}.

The modified Fisher-Tropsch catalysts include Cu-Fe and Cu-Co based catalysts, of which Cu-Fe catalysts tend to initiate water gas shift reaction (WGS) and thus generate more CO₂. Comparatively, Cu-Co based catalysts show good performance for HAS at mild reaction conditions, and become one of the most promising

^a Collaborative Innovation Center of Chemical Science and Engineering (Tianjin), Tianjin 300072, China. Email: yuanliu@tju.edu.cn. Tel: +86 022 87401675.

^b Tianjin Key Laboratory of Applied Catalysis Science and Technology, School of Chemical Engineering, Tianjin University, Tianjin 300072, China.

catalysts for practical application.

For Cu-Co based catalysts, copper acts as the active site for the non-dissociative adsorption of CO and the dissociative chemisorption of H₂; while cobalt is responsible for the dissociative activation of CO and carbon chain growth. Therefore, the synergistic working of the copper and cobalt sites can promote the generation of higher alcohols¹¹⁻¹³. It is acknowledged that the formation of Cu-Co alloy is beneficial for the synergistic catalyzing. Hence the formation of Cu-Co alloy is important for HAS, and the formation of Cu-Co alloy can increase the selectivity to C₂₊ alcohols¹⁴⁻¹⁷.

In order to form Cu-Co alloy, CuCoO₂¹⁸ and CuCo₂O₄^{14,19} were used as the precursors, in which cobalt and copper ions are uniformly distributed at the atomic level. Consequently, the formation of Cu-Co alloy should be favored in the reduction process. However supported catalysts generally are prepared by impregnation method followed by drying and calcination. During the impregnation process, making the metal species being uniform and highly dispersed on the support is vital to the performance of catalyst. There are many influencing factors, such as the interaction between the metal ions with the support, the migration and aggregation of the metal species during the drying and calcination processes. Thus, in the resulting supported Cu-Co based catalysts, apart from CuCoO₂ and CuCo₂O₄, CuO and Co₃O₄ would be inevitably formed. After reduction, mono metal particles of copper and cobalt derived from CuO and Co₃O₄ would be generated, reducing the selectivity to C₂₊ alcohols by producing methanol and hydrocarbons, respectively.

Layered double hydroxides (LDHs), a class of synthetic two-dimensional nanostructured layered materials²⁰⁻²², have recently received significant attentions owing to their promising applications as heterogeneous catalysts²³⁻²⁵ and catalyst supports²⁶. LDHs can be expressed by a typical formula [M²⁺_{1-x}M³⁺_x(OH)₂]^{x+} (Aⁿ⁻)_{x/n}mH₂O, where M²⁺ and M³⁺ are divalent and trivalent

cations, respectively. Aⁿ⁻ is the interlayer anion, to make electrical neutrality with the cations. In LDHs, the metal cations of M²⁺ and M³⁺ are uniformly distributed at atomic level in the brucite-like layers. A character of LDHs is that the uniform distribution of the metal species would be maintained in the resultant mixed metal oxides after calcination although the LDHs structure would be destroyed, which is owing to the topological effect of LDHs^{27,28}. The uniform distribution of the metal species in the mixed metal oxides and the topological effect of LDHs are beneficial and crucial for preparing supported nano metal alloy

Studies on bimetallic catalysts prepared via LDHs as the precursors can be found. For instance, Li *et al.*²⁴ prepared Co-Ni based catalysts by calcinating and reducing LDHs precursors, which exhibited high activity and good stability for ethanol steam reforming. Yang *et al.*²⁹ reported that uniform Co-Fe alloy nanoparticles with a narrow size distribution were obtained by reducing the LDHs precursors which contain Mg, Co and Fe ions. However, to the best of our knowledge, using the LDHs as the precursor to prepare supported nanoparticles of Cu-Co alloy for HAS has not been reported.

In the present investigation, Cu-Co alloy nanoparticles supported on Al₂O₃ were prepared by using LDHs as the precursor. The resulted catalysts showed good catalytic performance for HAS from syngas, especially exhibited high selectivity to C₂₊ alcohols.

2. Experimental

2.1 Materials

Analytical grade chemicals of Cu(NO₃)₂•3H₂O, Co(NO₃)₂•6H₂O, Al(NO₃)₃•9H₂O, NaOH and Na₂CO₃ were purchased from Aladdin and used without further purification. Deionized water was used in all the experimental processes.

2.2 Preparation of Cu-Co catalysts

A series of (Cu_xCo_y)₂Al-LDHs ([Cu²⁺] +

$[\text{Co}^{2+}]/[\text{Al}^{3+}] = 2$ in molar) with Cu/Co molar ratio of 1:0, 1:1, 1:2, 1:3 and 0:1 was prepared by a co-precipitation method. $\text{Cu}(\text{NO}_3)_2 \cdot 3\text{H}_2\text{O}$, $\text{Co}(\text{NO}_3)_2 \cdot 6\text{H}_2\text{O}$ and $\text{Al}(\text{NO}_3)_3 \cdot 9\text{H}_2\text{O}$ were dissolved in deionized water at $[\text{Cu}^{2+}] + [\text{Co}^{2+}] + [\text{Al}^{3+}] = 1.0$ M. NaOH and Na_2CO_3 were dissolved in deionized water with $[\text{NaOH}] = 1.5$ M and $[\text{CO}_3^{2-}] = 2[\text{Al}^{3+}]$. The two solutions were simultaneously added into deionized water under vigorous stirring, maintaining $\text{pH} = 9.5 \pm 0.1$. As the precipitation was completed, the slurry was aged at 80°C for 12 h, and then filtered, washed with distilled water and dried at 70°C for 12 h. The thus prepared LDHs were calcined at 500°C for 3 h, denoted as $(\text{Cu}_x\text{Co}_y)_2\text{Al-CLDHs}$, and then reduced at 450°C for 3 h in hydrogen. The reduced catalysts were named as $(\text{Cu}_x\text{Co}_y)_2\text{Al-Red}$.

2.3 Catalyst characterization

The phase analyses of the catalysts were determined by the X-Ray Diffraction (XRD) technique which was recorded on an X'Pert Pro instrument, a Co K α radiation source was used with an accelerating voltage of 40 kV and electric current of 40 mA. The spectrum was collected at a scanning speed of 5°min^{-1} .

Nitrogen adsorption and desorption isotherms were performed on a Trwastar 3000 micromeritics apparatus at -196°C . The specific surface areas were calculated based on the BET method and the pore size distributions were calculated from the adsorption branch of the isotherms using the BJH model. All samples were outgassed under vacuum at 300°C for 4 h prior to analysis.

Scanning electron microscopy (SEM) characterizations were performed on a Hitachi S-4800 field-emission scanning electron microscope to observe the morphology of the samples, which were treated with Au sputtered first.

Transmission electron microscopy (TEM) pictures and high angle annular dark field scanning transmission electron microscopy (HAADF-STEM) line scans combined with energy dispersive X-ray spectroscopy

(EDX) for the determination of metal composition and elemental mapping were obtained on a JEOL JEM-2100F microscope field-emission transmission electron microscope. After ultrasonic dispersion of the catalysts in absolute ethanol, the well-dispersed samples were dropped and dried on a Mo grid with a layer of holey carbon film.

Temperature programmed reduction (TPR) tests were carried out on a fixed bed micro-reactor in order to study the reducibility of the metal species in the catalysts. In each run, 50 mg of the catalyst was loaded into a quartz tube reactor and pretreated with 5% H_2/Ar to remove the air in the reactor at room temperature. Then, the catalyst was heated from room temperature to 800°C at a heating rate of 10°Cmin^{-1} in the presence of 5% H_2/Ar flow at a flow rate of 48 mL min^{-1} .

2.4 Catalyst characterization

The higher alcohols synthesis tests were conducted in a fixed-bed, stainless flow micro-reactor with a length and inner diameter of 300 nm and 8 mm, respectively. 800 mg of catalyst with 40-60 mesh grain size was diluted with 3200mg quartz sand with the same size and then loaded into the reactor, the mass ratio of the catalysts and quartz sand was 1:4. All catalysts were activated on-line under a flow of H_2 at 450°C for 3 h at a rate of 2°C min^{-1} . Subsequently, the reactor was cooled to room temperature, and the pressure was increased to 3 MPa by feeding the syngas mixture ($\text{H}_2/\text{CO}/\text{N}_2 = 8:4:1$, where N_2 was used as the internal standard gas for analyzing the reacted gases). The gas hourly space velocity was set at $3900 \text{ mL (g}_{\text{cat}}\text{h)}^{-1}$. At each reaction temperature from 250 to 290°C , the reaction was maintained for 1.5 h to obtain steady-state activity and selectivity; except at 240°C the reaction was conducted for 3 h. A gas chromatograph with two packed columns was used to analyze the products. The gas products of CO , H_2 , CH_4 , CO_2 and N_2 were separated online using a TDX-01 packed column (2 m) connected to a TCD detector. After separation by condensation, liquid products and hydrocarbons were analyzed off-line using a

ARTICLE

Porapak Q column (3 m) connected to a FID detector.

CO conversion (X_{CO}) and the product selectivity (S_i) were calculated according to the following

$$\text{equations: } X_{CO} = \frac{CO_{in} - CO_{out}}{CO_{in}} \times 100\%$$

$$S_i = \frac{nC_i}{\sum nC_i} \times 100\%$$

Where CO_{in} , CO_{out} is the moles of CO in the feed-gases and off-gases, respectively; n , C_i represents the number of carbon atoms in the molecule and moles of a carbon-containing product, respectively.

3. Results and discussion

3.1 XRD

The XRD patterns of as-synthesized $(Cu_xCo_y)_2Al$ -LDHs are shown in Fig. 1(I). All samples show sharp and symmetric diffractions at 2θ values of 13.5, 27.2 and 40.5°, ascribed to the crystalline planes of (003), (006) and (009) for LDHs, respectively, indicating well-crystallized hydroxalcalite structures. No any detectable impurity phases can be observed, indicating the high purity of LDHs structure in the samples.

Particularly, the XRD patterns show a variation trend correlated to the chemical compositions. With the increase content of copper, the diffraction peaks moves to a little higher 2θ values (Fig. 1(I) inset). This is attributed to the distortion of copper ions in LDHs as pointed by Khan *et al.*³⁰. Similarly, Liu *et al.* also pointed out that Cu^{2+} ions in LDHs showed Jahn-Teller effect that favored the formation of distorted octahedral structure³¹, which lead to the shift of the diffraction peaks. Compared with copper ion, cobalt ion is easier to form LDHs structure, thus the two diffraction peaks of (110) and (113) at 2θ values of around 71 and 74° become sharper and stronger with cobalt content increasing.

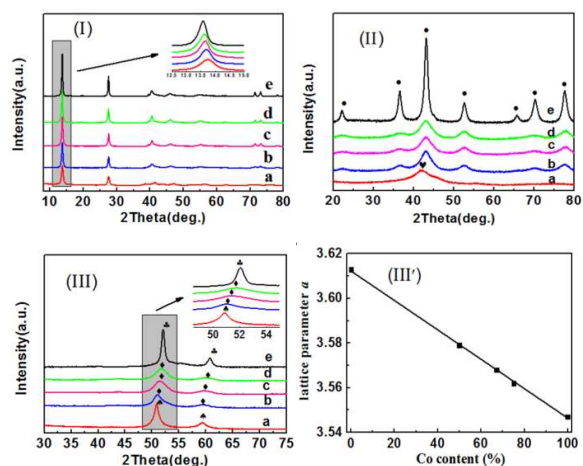


Fig. 1 XRD patterns of (I) $(Cu_xCo_y)_2Al$ -LDHs, (II) $(Cu_xCo_y)_2Al$ -CLDHs and (III) $(Cu_xCo_y)_2Al$ -Red with x/y ratios of (a) 1:0, (b) 1:1, (c) 1:2, (d) 1:3 (e) 0:1. Crystalline phases: (●) $Co_3O_4/CuCo_2O_4$, (♥) CuO , (♣) Co , (♠) Cu , (♦) $Cu-Co$ alloy; (III') the variation of Cu/Co molar ratio vs. lattice parameter a .

The basic spacing (d_{003}), varies between 0.746 and 0.752, which is close to the values for CO_3^{2-} containing LDHs with M^{2+}/Al^{3+} ratio of about ~ 2 ³². Thus, CO_3^{2-} was successfully introduced into the space between the hydroxalcalite laminates.

Fig. 1 (II) shows the XRD patterns of $(Cu_xCo_y)_2Al$ -CLDHs. It can be seen that the diffraction peaks corresponding to LDHs disappear, and the diffraction peaks of metal oxides appear, suggesting that the LDHs structures are completely destroyed and transformed into metal oxides after calcination. In addition, the diffraction peaks corresponding to Al_2O_3 cannot be observed, indicating that Al_2O_3 is in amorphous state.

For the Cu_2Al -CLDHs, only a peak attributed to CuO crystalline phase at $2\theta = 41.4^\circ$ exists, and the peak is broad, meaning a small size of the CuO nanoparticles.

As for the cobalt containing samples, the diffraction peaks corresponding to CuO phase can hardly be seen, which is attributed to the following two reasons. One is that the copper and cobalt species are combined to form $CuCo_2O_4$ during calcination, which is supported by the presence of the characteristic diffraction peaks of $CuCo_2O_4$. The other is that the left copper species in CuO phase are

highly dispersed or in small quantity. As the atomic ratio of Cu/Co equals to 0.5, which is the stoichiometric ratio of Cu/Co in CuCo_2O_4 , copper should be mainly in CuCo_2O_4 . As further increasing cobalt content, CuCo_2O_4 and Co_3O_4 are the major phases in the catalyst. This is revealed by the slight shift of the lattice parameter from 8.105 Å of pure CuCo_2O_4 to 8.101 Å. Both CuCo_2O_4 and Co_3O_4 belong to spinel structure, while the lattice parameter of Co_3O_4 is slightly smaller due to the smaller size of cobalt ion. Finally, Co_3O_4 becomes the only oxide with spinel phase for $\text{Co}_2\text{Al-CLDHs}$ catalyst.

In summary, copper and cobalt exists in CuCo_2O_4 accompanied with CuO or Co_3O_4 in the calcined catalysts, and copper and cobalt existed mainly in CuCo_2O_4 for $(\text{Cu}_1\text{Co}_2)_2\text{Al-CLDHs}$.

In addition, all of the diffraction peaks are broad, suggesting that the crystal grains are small. The metal oxides in the calcined samples came from LDHs, where the metal ions were uniformly mixed at atomic level, so the metal oxides should be uniformly mixed. In other words, CuCo_2O_4 , CuO and Co_3O_4 were well mixed and highly dispersed on the amorphous Al_2O_3 matrix. The nanoparticles of the oxides should be in interaction, which further limited the migration and aggregation of those oxides. This means that the resulted mixed oxide possesses high anti-sintering ability, which agrees with the results in the literature³³, where $\text{ZnO/ZnAl}_2\text{O}_4$ nanocomposite was made by using LDHs as the precursor and exhibited high thermal stability.

Fig. 1 (III) shows the XRD results of reduced catalysts. For $\text{Co}_2\text{Al-Red}$ and $\text{Cu}_2\text{Al-Red}$, diffraction peaks corresponding to metal cobalt and copper can be seen clearly. No diffraction peak related to alumina can be detected, showing alumina is in amorphous state.

For $(\text{Cu}_x\text{Co}_y)_2\text{Al-Red}$ containing both copper and cobalt elements, diffraction peaks corresponding to copper and cobalt containing oxides disappear, while peaks between the diffraction peaks of pure metal Cu and Co are

observed, which can be clearly seen from the inset picture in Fig. 1 (III). Su *et al.*³⁴ attributed the diffraction peaks between pure metal Co and Cu to the bimetallic Co-Cu alloy. Volkova *et al.*¹⁸ demonstrated that the slight increase in lattice spacing for copper and a small decrease in lattice spacing for cobalt are the characteristics of the Co-Cu alloy. Hence, Cu-Co alloy was formed in $(\text{Cu}_x\text{Co}_y)_2\text{Al-Red}$.

As shown in Fig. 1 (III'), the metal lattice parameter of a for $(\text{Cu}_x\text{Co}_y)_2\text{Al-Red}$ is smaller than that of Cu^0 (3.613 Å), larger than that of Co^0 (3.548 Å), and decrease linearly with the increase of cobalt content. This is in accordance with that the size of cobalt atom is smaller than that of copper, supporting the formation of Cu - Co alloy³⁵⁻³⁷. Vegard's law³⁵ pointed out that independent of other factors, the microscopic crystal structures of alloys depend on the atomic sizes and relative concentrations of the constituent. For Cu-Co alloy, the lattice parameter a should decrease linearly with increasing Co content due to the smaller size of cobalt than that of copper, and vice versa, the linearly variation is an indication for the Cu-Co alloy formation.

Although some CuO and Co_3O_4 were formed inevitably after calcination of LDHs, considering that the metal ions are uniformly distributed in an atomic level in the layers of LDHs, all the CuO , Co_3O_4 and CuCo_2O_4 with small and uniform particle sizes were mixed evenly on the amorphous Al_2O_3 matrix. Thus the interaction between them should be enhanced, and consequently, Cu-Co alloy rather than separate copper and cobalt are formed after reduction.

3.2TPR

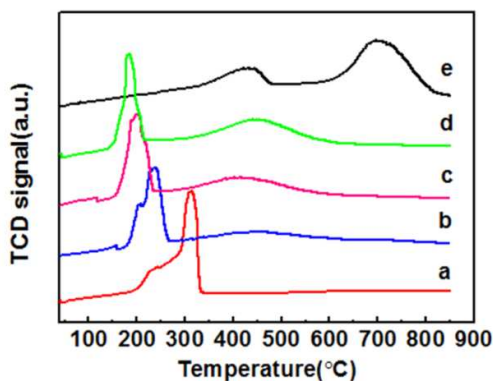


Fig. 2 TPR patterns of catalysts of (a) $\text{Cu}_2\text{Al-CLDHs}$, (b) $(\text{Cu}_1\text{Co}_1)_2\text{Al-CLDHs}$, (c) $(\text{Cu}_1\text{Co}_2)_2\text{Al-CLDHs}$, (d) $(\text{Cu}_1\text{Co}_3)_2\text{Al-CLDHs}$ and (e) $\text{Co}_2\text{Al-CLDHs}$.

The TPR profiles of the calcined catalyst are shown in Fig. 2. For $\text{Co}_2\text{Al-CLDHs}$, two reduction peaks in the temperature range of 310 - 410 °C and 600 - 780 °C are observed, according to previous reports^{14, 38, 39}, which should be attributed to the reduction of Co_3O_4 to CoO and CoO to metallic cobalt, respectively. The H_2 consumption ratio of the two peaks is close to 1:3, which supports the attribution. This result also suggests that cobalt species are mainly in Co_3O_4 state, in consistent with XRD results.

A.Y. Khodakov *et al.*⁴⁰ stated that for the interaction between metal oxide and support the smaller the particle is, the stronger the interaction, and thus the metal oxide with smaller size is harder to be reduced. Compared with that of Co_3O_4 reported by Chu *et al.*⁴¹, the reduction temperature of Co_3O_4 in $\text{Co}_2\text{Al-CLDHs}$ is higher, which is likely due to the smaller size of Co_3O_4 in $\text{Co}_2\text{Al-CLDHs}$.

For $\text{Cu}_2\text{Al-CLDHs}$, two reduction peaks centering at around 220 and 300 °C can be observed, corresponding to the reduction of CuO to metallic Cu, as reported in the literature⁴². The peak at the lower temperature can be attributed to the reduction of highly dispersed CuO and the other is ascribed to CuO which in strong interaction with the Al_2O_3 support.

For $(\text{Cu}_x\text{Co}_y)_2\text{Al-CLDHs}$, the reduction peaks at about 450 °C should belong to the reduction of cobalt ions. The reasons are as follows. Firstly, copper ions could be

reduced at much lower temperature, seeing the reduction profile for $\text{Cu}_2\text{Al-CLDHs}$. Secondly, the area of this reduction peak increases with the content increase of cobalt in the catalyst. As compare to $\text{Co}_2\text{Al-CLDHs}$, the reduction temperature of this peak for cobalt oxide is obviously lower, which is ascribed to the formation of metal Cu-Co at the lower reduction temperatures. It is known that metal particles can activate hydrogen and catalyze the reduction of metal ions nearby^{43,44}.

For $(\text{Cu}_x\text{Co}_y)_2\text{Al-CLDHs}$, the reduction peaks in temperature range of 150 to 250 °C are corresponding to the formation of bimetal Cu-Co. Compares to the reduction profiles of $\text{Co}_2\text{Al-CLDHs}$ and $\text{Cu}_2\text{Al-CLDHs}$ (Fig. 2 a and e), the reduction temperatures of $(\text{Cu}_x\text{Co}_y)_2\text{Al-CLDHs}$ (Fig. 2 b, c and d) are obviously lower. The difference between them is that $(\text{Cu}_x\text{Co}_y)_2\text{Al-CLDHs}$ contains CuCo_2O_4 , and CuCo_2O_4 is the main phase for $(\text{Cu}_x\text{Co}_y)_2\text{Al-CLDHs}$ as the above XRD results shown. Thus, the reduction peaks in the temperature range of 150 to 250 °C are attributed to the reduction of CuCo_2O_4 to metal copper and metal cobalt.

The XRD results indicate that, besides CuCo_2O_4 , there are Co_3O_4 and CuO in $(\text{Cu}_x\text{Co}_y)_2\text{Al-CLDHs}$. The reduction of the CuO can be included in the reduction peaks at 150 to 250 °C, for that the bimetal of Cu-Co reduced from CuCo_2O_4 can catalyze the reduction of copper ions, resulting into the decrease of reduction temperature for CuO. The Co_3O_4 may be partly reduced at the temperature range of 150 to 250 °C for the cobalt species weakly interacted with alumina, and partly reduced at about 450 °C for the cobalt species interacted with alumina.

To note the reduction profiles of $(\text{Cu}_x\text{Co}_y)_2\text{Al-CLDHs}$, copper and cobalt ions would be reduced to metallic state simultaneously at 150 to 250 °C. The XRD results and the properties of the LDHs precursor suggest that copper and cobalt species in $(\text{Cu}_x\text{Co}_y)_2\text{Al-CLDHs}$ are uniformly and highly dispersed in small size (see Tab. 1). The simultaneously generated metal copper and metal cobalt

grains, which are in small size and uniformly mixed, should inclined to form Cu-Co alloy.

3.3BET

Fig. 3 (I) shows the N_2 adsorption-desorption isotherms and the corresponding pore size distribution of $(Cu_xCo_y)_2Al$ -CLDHs. All samples exhibit a typical IV isotherm with an H_3 -type hysteresis loop, suggesting the presence of mesopores. This result is further confirmed by the corresponding pore size distribution in Fig. 3 (II).

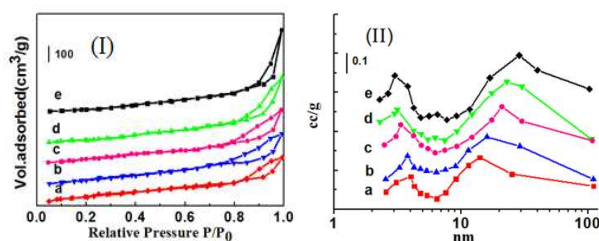


Fig. 3 N_2 adsorption-desorption curves (I) and pore size distributions (II) of (a) Cu_2Al -CLDHs, (b) $(Cu_1Co_1)_2Al$ -CLDHs, (c) $(Cu_1Co_2)_2Al$ -CLDHs, (d) $(Cu_1Co_3)_2Al$ -CLDHs and (e) Co_2Al -CLDHs.

As can be seen from the pore size distribution, there are two main pore size distributions in the calcined catalysts. One is meso pores in size of several nanometers, and the other in size of tens nanometers. The former is proposed to be formed from the left of CO_3^{2-} and water in LDHs in the calcination process, and the latter came from the accumulation of oxides particles. From the SEM images, it is seen the particle size is in tens nanometer, in accordance for accumulating the pores. The similar view point has been stated in the literatures^{28, 45}.

For more detail, the pores formed from the left of

Table 1 Physical properties and crystal sizes of the catalysts

Samples	BET surface Area ($m^2 g^{-1}$)	BJH pore Volume ($cm^3 g^{-1}$)	Pore diameter (nm)	Crystal Size ^a (nm)	Crystal Size ^b (nm)
Co_2Al -CLDHs	137	0.47	3.03	23.2	17.8
$(Cu_1Co_3)_2Al$ -CLDHs	123	0.45	3.14	7.2	4.3
$(Cu_1Co_2)_2Al$ -CLDHs	106	0.39	3.35	8.4	4.8(6.2 ^c)
$(Cu_1Co_1)_2Al$ -CLDHs	90	0.33	3.80	9.3	5.1
Cu_2Al -CLDHs	61	0.26	4.02	4.7	15.4

^a Crystal sizes of the catalysts after calcination were calculated by X-ray diffraction with Scherrer equation. ^b Crystal sizes of the catalysts after reduction were calculated by X-ray diffraction with Scherrer equation. ^c Data for the catalyst after 200 hours' stability test.

CO_3^{2-} and water can be divided into two categories. CO_3^{2-} ions were located between the sheets of LDHs, thus CO_3^{2-} leaving would cause slit-shaped pores between the sheets; while water in the state of hydroxyls is in the sheets of LDHs, thus water leaving would result micro and meso pores in the sheets. By the way, due to the topological property of the LDHs, the calcined samples maintain the morphology, that is, the shape of sheet was preserved. On the whole, the pores mainly came from the accumulation of particles, the accumulation of the oxide sheets formed the slit-shaped pores in several nanometer size, and the accumulation of the sheets constituted the larger particles in tens nanometer which stacked and formed larger pores. This means that the surface area mainly came from the particles, hence no evident capillary condensation is exhibited in the sorption isotherms of Fig. 3.

The hierarchical porous structure should play a favorable role on the higher alcohols synthesis. Ding *et al.*⁴⁶ found that Cu-Fe supported on the bimodal porous SiO_2 exhibited good catalytic activity and high selectivity to C_2+OH , which was attributed to the well dispersion of active metal sites and high diffusion efficiency of products inside the bimodal porous structure. Lu *et al.*⁴⁷ found that three-dimensionally ordered macroporous Cu-Fe catalysts showed high activity and selectivity to C_2+OH , because of the unique ordered porous structure of the catalysts, the uniformly distributed active components and the synergetic effect between Cu and χ - Fe_5C_2 .



RSC Advances

ARTICLE

The specific surface areas and the pore structure parameters are shown in Table 1. The BET surface areas ranged in $61\text{--}137\text{ m}^2\text{ g}^{-1}$ and the pore volumes in $0.26\text{--}0.47\text{ cm}^3\text{ g}^{-1}$. The specific surface area and pore volume decreases with the increase of copper content, which may be due to the different shape. With increasing cobalt content, the shape of particles changed from cubic or rectangle to platelet, see SEM images in Fig. 4a–4c, and the platelets have higher specific surface area. The shape difference of the morphology is likely due to the Jahn-Teller effect of Cu^{2+} ions, as pointed in the literature³¹.

3.4 SEM

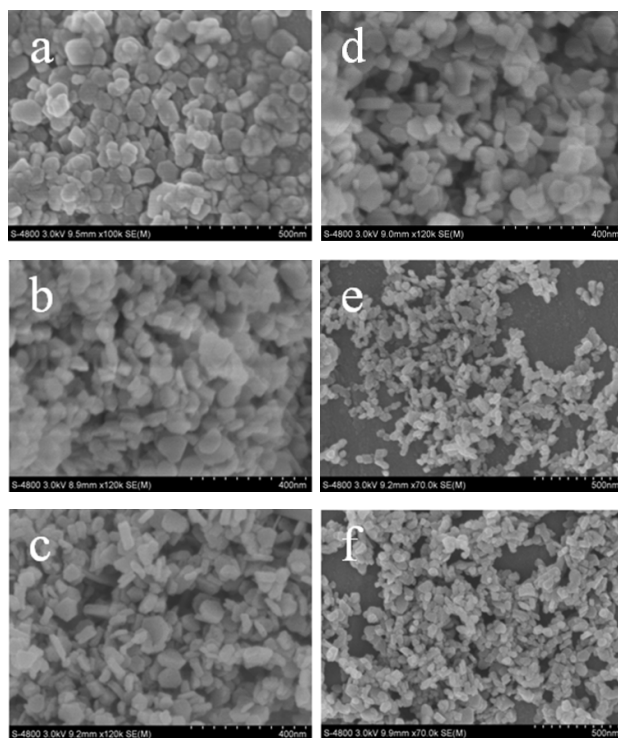


Fig. 4 SEM images of (a) $\text{Cu}_2\text{Al-LDHs}$, (b) $(\text{Cu}_1\text{Co}_1)_2\text{Al-LDHs}$, (c) $\text{Co}_2\text{Al-LDHs}$, (d) $(\text{Cu}_1\text{Co}_2)_2\text{Al-LDHs}$, (e) $(\text{Cu}_1\text{Co}_2)_2\text{Al-CLDHs}$ and (f) $(\text{Cu}_1\text{Co}_2)_2\text{Al-Red}$.

The morphology of the samples was investigated by

SEM as shown in Fig. 4. The LDHs precursors display smooth and uniform nanocrystals with a narrow particle size distribution of 30–70 nm. Owing to the topological effect of hydrotalcite, when the LDHs was calcined and reduced, the same morphology to LDHs was still maintained, while the particle sizes became smaller than that of the precursors, see Fig. 4d–4f. The similar morphology of the samples after calcination and reduction with LDHs confirmed the existence of the topological effect, supporting the above viewpoint that CuO , Co_3O_4 and CuCo_2O_4 would be mixed evenly in the Al_2O_3 matrix, as a result, the formation of Cu-Co alloy are favored after reduction.

3.5 TEM

TEM pictures are presented in Fig. 5(a). A representative high resolution TEM image is shown in the inset picture in Fig. 5 (a), and the lattice space of 2.08 \AA is corresponding to the (110) crystal plane of Cu-Co alloy, suggesting the formation of Cu-Co alloy, which is consistent with the XRD results in Fig. 1 (III).

It can be seen from Fig. 5 (a) that the Cu-Co alloy nanoparticles are evenly distributed throughout the amorphous Al_2O_3 matrix without severe aggregation and exhibit a uniform spherical-like shape. In addition, the average sizes of Cu-Co alloy nanoparticles range from 3.5 to 7 nm, to see the inset of particle size distribution in Fig. 5 (a), agrees with the average crystallite size calculated from the XRD (listed in Tab. 1). The narrow particle size distribution is attributed to the uniform distribution of copper and cobalt ions in its precursor and to the effective prevention of the Al_2O_3 matrix to the alloy particle sintering.

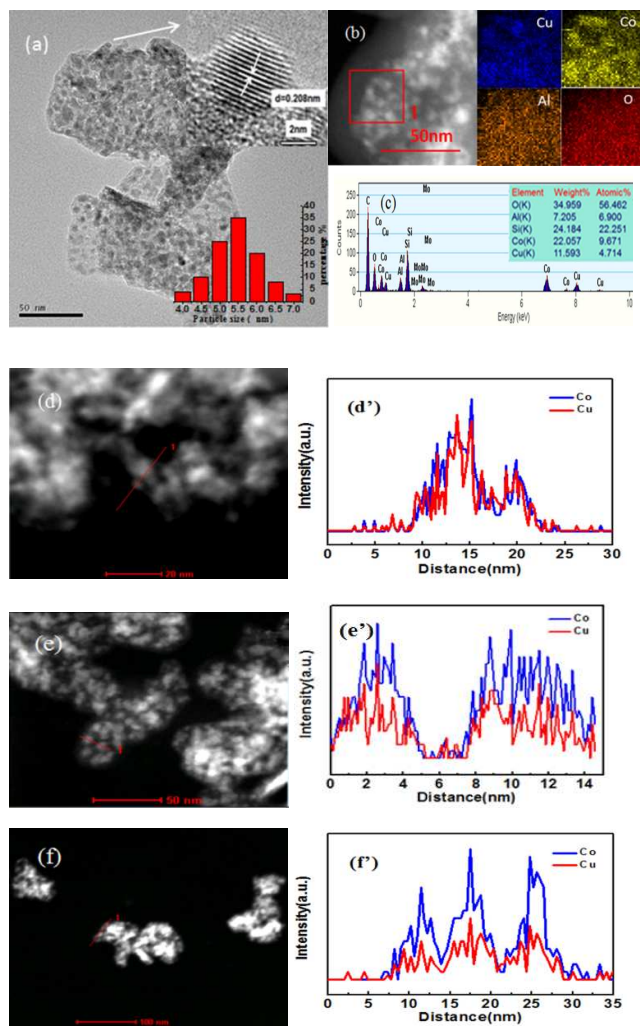


Fig. 5 (a) TEM (insets: a HRTEM image and the particle size distribution diagram), (b) EDX mapping, (c) EDX spectrum of the $(\text{Cu}_1\text{Co}_2)_2\text{Al-Red}$ observed on a Mo substrate. Si comes from quartz sand. STEM images and the corresponding EDS line scanning profiles for Cu and Co elements of (d) and (d') $(\text{Cu}_1\text{Co}_1)_2\text{Al-Red}$, (e) and (e') $(\text{Cu}_1\text{Co}_2)_2\text{Al-Red}$, (f) and (f') $(\text{Cu}_1\text{Co}_3)_2\text{Al-Red}$.

For further insight into the distribution of copper and cobalt, Energy Dispersive X-ray Spectrometry Mapping Analysis (Fig. 5(b)) was performed. Noting that, Cu and Co show the same morphology of distribution, meaning the uniform and homogeneous distribution of Cu and Co elements throughout the Al_2O_3 matrix. The energy dispersive X-ray spectrometry (EDX) analysis in Fig. 5 (c) for $(\text{Cu}_1\text{Co}_2)\text{Al-Red}$ reveals the co-existence of Cu, Co and Al elements, and the Cu/Co and (Cu+Co)/Al molar ratio are 0.49 and 2.08, respectively, which is in good

accordance with that in the initial nitrate salt for preparing the precursor.

Atomic-scale chemical composition across $(\text{Cu}_x\text{Co}_y)_2\text{Al-Red}$ were investigated by HAADF-STEM-EDS line scans, representative images and EDS curves are shown in Fig. 5d-f and d'-f'. The red lines in Fig. 5d-f in the STEM pictures are the scanning area, which is corresponding to the EDS curves in Fig. 5d'-f'. The same variation tendency for the two elements of copper and cobalt can be seen clearly, meaning the formation of homogeneous Cu-Co alloy in all the three catalysts. Noting that the intensity of the signal for copper and cobalt is different in different samples, indicating the formed Cu-Co alloy with different Cu/Co ratio, which is in good accordance with the XRD and TPR results.

Studies on the phase diagram of binary Co-Cu suggest that the maximum solubility of copper in metal cobalt is 9 % in molar ratio⁴⁸. It should be noted that this solubility is for the bulk alloy, that is, for the alloy with large crystalline size. While for the nanosized bimetallic Cu-Co, the situation should be different. Prieto *et al.*¹⁶ demonstrated that the superior nanoscale mixing of Cu and Co species can promote the formation of Cu-Co alloy nanocrystals after activation, and pointed that the maximum occurrence of the Cu-Co alloy phase is at a Cu/Co molar ratio of 0.5. Volkova *et al.*¹⁸ also found single-phase Cu-Co alloy with the alloy composition $\text{Cu}_{0.5}\text{Co}_{0.5}$ after low-temperature reduction of CuCoO_2 .

3.6 Catalytic performance

In the process of higher alcohols synthesis from syngas over CuCo-based catalysts, several parallel reactions including Fischer-Tropsch synthesis and water-gas-shift reaction (WGSR) can be occurred. It is widely accepted that HAS requires both dissociative and non-dissociative activation of CO on different active sites. Cu can act as the active sites for CO molecular activation and insertion, while Co for CO dissociative activation and chain propagation. An appropriate balance between CO

ARTICLE

Journal Name

dissociation and CO insertion was suggested to be necessary for the synthesis of higher alcohols. So the synergetic effect of homogeneously dispersed copper and cobalt species plays a key role in the catalytic performance.

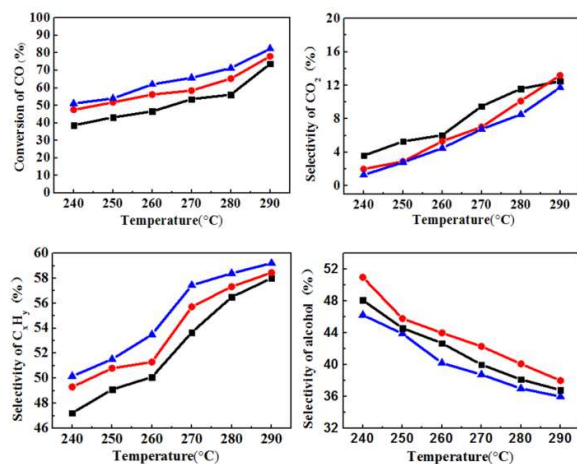


Fig. 6 The conversions of CO and selectivity toward hydrocarbons, CO₂ and alcohols vs reaction temperature over (■) (Cu₁Co₁)₂Al-Red, (●) (Cu₁Co₂)₂Al-Red and (▲) (Cu₁Co₃)₂Al-Red at GHSV of 3900 mL (g_{cat} h)⁻¹ in the syngas mixture of H₂/CO/N₂ = 8/4/1 and at 3 MPa.

Fig. 6 shows the results of catalytic performance over (Cu_xCo_y)₂Al-Red catalysts with different Cu/Co ratio. It is shown that the conversion of CO and the selectivity towards hydrocarbons increase with increasing cobalt content and the reaction temperature over the three catalysts. This agrees with the fact that metallic Co⁰ is the active component for F-T reaction, and is responsible for the dissociative CO adsorption, C-C chain growth and hydrogenation. The selectivity of hydrocarbons increasing with reaction temperature is ascribed to the high activation energy for the dissociative adsorption of CO, which is favorable for hydrocarbon generation at higher temperatures^{3,15}.

With the increase of copper content, the level of CO₂ production increase accordingly. This is in accordance with the fact that Cu is more active than Co for WGS⁴⁹. In addition, an increased selectivity towards CO₂ with increasing reaction temperatures can be observed for all

samples. The formation of alcohols and hydrocarbons are accompanied with the production of water, and water reacted with CO via WGS⁵⁰ generated CO₂. With the temperature increase, the content of water increased markedly with the increase of CO conversion, in turn accelerating WGS and CO₂ generation.

The catalytic performance results present in Table 2. The selectivity to higher alcohols increased from 42.3% of Cu/Co = 1:3 to 44.1% of Cu/Co = 1:2, and then went down to 42.6% of Cu/Co = 1:1. (Cu₁Co₂)₂Al-Red exhibit the highest selectivity toward higher alcohols, likely owing to that in which most copper and cobalt were in the state of alloy, to note that the ratio of Cu/Co in (Cu₁Co₂)₂Al-Red equals to that in CuCo₂O₄.

It is worth mentioning that the selectivity toward higher alcohols is higher than that over previously reported Cu-Co-based catalysts^{14,51}, which should be due to the formation of Cu-Co alloy and the uniform mixing of the elements in the catalyst. In the alloyed phase, the two active sites are uniformly distributed and extremely close to each other. This can significantly increase the synergistic effect between copper and cobalt, which contributed to the enhancement of the selectivity to higher alcohols, as stated in the literatures^{14,16,34}.

Over (Cu₁Co₂)₂Al-Red and at 250°C, 3MPa and GHSV of 3900 mL(g_{cat}h)⁻¹, CO conversion is 51.8%, the selectivity to alcohols is 45.8%, and 94.3 wt. % of the alcohols is C₂₊-OH. The catalyst is very active and especially exhibited much high selectivity to C₂₊-OH.

The stability test results for (Cu₁Co₂)₂Al-Red are shown in Fig. 7. The CO conversion and the selectivity to alcohols substantially remain stable in the 200 hours' reaction process. After reaction for 200 h, the conversion of CO is 53.1%, the selectivity to alcohols is 38.4%, and the mass fraction of higher alcohols in total alcohols is 92.8 wt.%.

Table 2 Catalytic performance of CO hydrogenation over $(\text{Cu}_x\text{Co}_y)_2\text{Al-Red}^a$.

Catalyst	X_{CO} %	S_{RH} %	S_{CO_2} %	ROH distribution			
				CH_3OH	$\text{C}_2\text{H}_5\text{OH}$	$\text{C}_3\text{H}_7\text{OH}$	C_4+OH
$\text{Cu}_2\text{Al-Red}$	35.7	11.8	8.5	76.2	2.1	0.9	0.5
$(\text{Cu}_1\text{Co}_1)_2\text{Al-Red}$	43.2	50.1	5.3	2.0	18.0	15.6	9.0
$(\text{Cu}_1\text{Co}_2)_2\text{Al-Red}$	51.8	51.3	2.9	1.7	18.3	16.9	8.9
$(\text{Cu}_1\text{Co}_3)_2\text{Al-Red}$	54.0	53.5	2.4	1.8	18.5	14.6	9.2
$\text{Co}_2\text{Al-Red}$	63.5	93.4	1.2	0.5	0.8	1.4	2.7

^a Reaction conditions: 250°C, GHSV = 3900 mL $(\text{g}_{\text{cat}} \text{h})^{-1}$, 3 MPa, $\text{H}_2/\text{CO}/\text{N}_2 = 8:4:1$.

Table 3 CO conversions, alcohols selectivities and the corresponding reaction conditions for some representative catalysts reported in references

Catalysts	Temperature (°C)	H_2/CO^a	Pressure (MPa)	GHSV (h^{-1})	X_{CO} (%)	S_{ROH} (%)	C_{2+}OH^b %
Co-Cu ⁴⁹	240	1.5	4	7200 ^c	5.7	37.9	37
Co@Cu ⁴²	230	2	2	18000 ^c	—	33.0	91.4
CuFeMg ²⁸	300	2	4	2000	56.89	49.1	77.0
Cu-Co/ Al_2O_3 ¹⁴	250	2	2	1800 ^c	23.2	23.3	79.3
Cu-Co/ Al_2O_3 ^d	250	2	2	1800 ^c	47.6	38.2	88.1
Cu-Co/ Al_2O_3 ^e	250	2	3	3900 ^c	51.8	45.8	94.3
Cu-Co/ Al_2O_3 ^f	260	2	3	3900 ^c	53.1	38.4	92.8

^a The molar ratio of H_2/CO . ^b The mass fraction of C_{2+}OH including ethanol in the total alcohols. ^c The unit is mL $(\text{g}_{\text{cat}} \text{h})^{-1}$. ^{d-e} In this work.^f

This work in stability test.

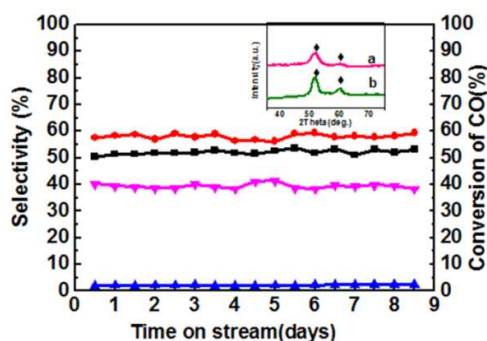


Fig. 7 Conversion of CO (■) and selectivity to alcohols (▼), hydrocarbons (●), CO_2 (▲) over $(\text{Cu}_1\text{Co}_2)_2\text{Al-Red}$ with reaction time on stream at $T = 260^\circ\text{C}$, $P = 3 \text{ MPa}$, $\text{GHSV} = 3900 \text{ mL } (\text{g}_{\text{cat}} \text{h})^{-1}$ and $\text{H}_2/\text{CO}/\text{N}_2 = 8/4/1$. The inset picture is the XRD profiles of (a) $(\text{Cu}_1\text{Co}_2)_2\text{Al-Red}$ and (b) $(\text{Cu}_1\text{Co}_2)_2\text{Al-Red}$ used for 200h, (◆) Cu-Co alloy.

The inset picture in Fig. 7 is the XRD profiles of (a) $(\text{Cu}_1\text{Co}_2)_2\text{Al-Red}$ and (b) $(\text{Cu}_1\text{Co}_2)_2\text{Al-Red}$ used for 200h. By comparing the diffraction peaks of Cu-Co alloy before and after 200h reaction, it is seen that the nanoparticles of Cu-Co alloy show good anti-sintering ability. The crystalline size only increased from about 4.8 nm the

catalyst before reaction to about 6.2 nm for the catalyst after the stability test.

The catalytic performance of some representative excellent catalysts reported in literatures is listed in Table 3. Taken activity and selectivity into consideration, Cu-Co alloy derived from $(\text{Cu}_x\text{Co}_y)_2\text{Al-LDHs}$ turns out to be one of the best catalysts for HAS. In particular, compared with that of Ref 14, under the same reaction conditions, the as-prepared catalysts in our work shows much better catalytic performance, whether the conversion of CO or the selectivity towards higher alcohols.

4. Conclusions

Layered double hydroxides containing copper, cobalt and aluminum ions with well crystallized hydroxalite structure were prepared by using co-precipitation method. After calcination, the resultant oxides particles were uniformly mixed in size of several nanometers and CuCo_2O_4 is one of the main phases, owing to the topological effect of LDHs. In the reduction process, the

ARTICLE

Journal Name

simultaneous reduction of copper and cobalt containing oxides and their well uniform mixing resulted in the formation of Cu-Co alloy. XRD, TEM and SEM results confirmed or supported the formation of Cu-Co alloy. By the way, the prepared catalysts possess dual pore size distribution structure ranged at several nanometers and tens nanometers.

The catalysts exhibited high activity and good stability for higher alcohols synthesis, especially showed very high selectivity to C₂₊ alcohols, which should be attributed to the formation of Cu-Co alloy and its high dispersion.

Acknowledgements

Financial support for this work was provided by the National Natural Science Foundation of China (NSFC) (Nos. 21376170, 21263011) is gratefully acknowledged.

Notes and References

- R. Zhang, G. Wang and B. Wang, *J. Catal.*, 2013, **305**, 238.
- J. Gong, H. Yue, Y. Zhao, S. Zhao, L. Zhao, J. Lv, S. Wang and X. Ma, *J. Am. Chem. Soc.*, 2012, **134**, 13922.
- G. Liu, T. Niu, D. Pan, F. Liu and Y. Liu, *Appl. Catal. A: Gen.*, 2014, **483**.
- L. Shi, W. Chu and S. Deng, *J. Nat. Gas. Chem.*, 2011, **20**, 48.
- K. Xiao, Z. Bao, X. Qi, X. Wang, L. Zhong, K. Fang, M. Lin and Y. Sun, *J. Mol. Catal. A: Chem.*, 2013, **378**, 319-325.
- E. Heracleous, E. T. Liakakou, A. A. Lappas and A. A. Lemonidou, *Appl. Catal. A: Gen.*, 2013, **455**, 145.
- J. Hu, Y. Wang, C. Cao, D. C. Elliott, D. J. Stevens and J. F. White, *Catal. Today*, 2007, **120**, 90.
- S. F. Zaman and K. J. Smith, *Catal. Today*, 2011, **171**, 266.
- D. Li, C. Yang, N. Zhao, H. Qi, W. Li, Y. Sun and B. Zhong, *Fuel Process. Technol.*, 2007, **88**, 125.
- H. Xiao, D. Li, W. Li and Y. Sun, *Fuel Process. Technol.*, 2010, **91**, 383.
- K. Fang, D. Li, M. Lin, M. Xiang, W. Wei and Y. Sun, *Cataly. Today*, 2009, **147**, 133.
- W. C. Siyu Deng and H. X. , Limin Shi, Lihong Huang, *J. Nat. Gas. Chem.*, 2007, **17**, 369.
- Y. Z. Fang, Y. Liu and L. H. Zhang, *Appl. Catal. A: Gen.*, 2011, **397**, 183.
- J. Wang, P. A. Chernavskii, A. Y. Khodakov and Y. Wang, *Journal of Catalysis*, 2012, **286**, 51-61.
- G. Liu, Y. Geng, D. Pan, Y. Zhang, T. Niu and Y. Liu, *Fuel Process. Technol.*, 2014, **128**, 289.
- G. Prieto, S. Beijer, M. L. Smith, M. He, Y. Au, Z. Wang, D. A. Bruce, K. P. de Jong, J. J. Spivey and P. E. de Jongh, *Angew Chem Int Ed.*, 2014, **53**, 6397.
- R. M. Bailliard-Letournel, A. J. Gomez Cobo, C. Mirodatos, M. Primet and J. A. Dalmon, *Cataly. Lett.*, 1989, **2**, 149.
- G. G. Volkova, T. M. Yurieva, L. M. Plyasova, M. I. Naumova and V. I. Zaikovskii, *J. Mol. Catal. A: Chem.*, 2000, **158**, 389.
- X. Dong, X.L. Liang, H.Y. Li, G.D. Lin, P. Zhang and H.B. Zhang, *Catal. Today*, 2009, **147**, 158.
- C. J. Wang and D. O'Hare, *J. Mater. Chem.*, 2012, **22**, 23064.
- J. L. Gunjakar, T. W. Kim, H. N. Kim, I. Y. Kim and S. J. Hwang, *J Am Chem Soc*, 2011, **133**, 14998.
- P. J. Sideris, U. G. Nielsen, Z. Gan and C. P. Grey, *Science*, 2008, **321**, 113.
- G. V. Manohara, D. A. Kunz, P. V. Kamath, W. Milius and J. Brey, *Langmuir*, 2010, **26**, 15586.
- L. He, H. Berntsen, E. Ochoa-Fernández, J. C. Walmsley, E. A. Blekkan and D. Chen, *Top. Catal.*, 2009, **52**, 206.
- A. I. Tsyganok, T. Tsunoda, S. Hamakawa, K. Suzuki, K. Takehira and T. Hayakawa, *J. Catal.*, 2003, **213**, 191.
- K. Xiao, X. Qi, Z. Bao, X. Wang, L. Zhong, K. Fang, M. Lin and Y. Sun, *Catal. Sci. Technol.*, 2013, **3**, 1591.
- C. Li, L. Wang, M. Wei, D. G. Evans and X. Duan, *J. Mater. Chem.*, 2008, **18**, 2666.
- W. Gao, Y. Zhao, J. Liu, Q. Huang, S. He, C. Li, J. Zhao and M. Wei, *Catal. Sci. Technol.*, 2013, **3**, 1324.
- S. Yang, L. Wang, S. Yue, Y. Lu, J. He and D. Zhao, *Dalton Trans*, 2014, **43**, 8254.
- A. I. Khan and O'Hare, *J. Mater. Chem.*, 2002, **12**, 3191.
- H. Liu, Q. Jiao, Y. Zhao, H. Li, C. Sun and X. Li, *J. Alloy Compd.*, 2010, **496**, 317.
- J.M. Oh, S.H. Hwang and J.H. Choy, *Solid State Ionics*, 2002, **151**, 285.
- X. Zhao, L. Wang, X. Xu, X. Lei, S. Xu and F. Zhang, *AIChE J.*, 2012, **58**, 573.
- J. Su, W. Mao, X.C. Xu, Z. Yang, H. Li, J. Xu and Y.F. Han, *AIChE J.*, 2014, **60**, 1797.
- A. R. Denton and N. W. Ashcroft, *Phys. Rev. A*, 1991, **43**, 3161.

Journal Name

ARTICLE

36. K. Takanabe, K. Nagaoka, K. Nariai and K. Aika, *J. Catal.*, 2005, **232**, 268.
37. F. Liu, Y. H. Qu, Y. Z. Yue, G. L. Liu and Y. Liu, *RSC Adv.* 2015, **5**, 16837.
38. Ø. Borg, M. Rønning, S. Storslter, W. van Beek and A. Holmen, *Stu. Surf. Sci. Catalysis.*, 2007, **163**, 255.
39. M. L. Smith, A. Campos and J. J. Spivey, *Catal. Today*, 2012, **182**, 60.
40. A. Y. Khodakov, A. Griboval-Constant, R. Bechara and V. L. Zholobenko, *J. Catal.*, 2002, **206**, 230.
41. W. Chu, P. Chernavskii, L. Gengembre, G. Pankina, P. Fongarland and A. Khodakov, *J. Catal.*, 2007, **252**, 215.
42. N. D. Subramanian, G. Balaji, C. S. S. R. Kumar and J. J. Spivey, *Catal. Today*, 2009, **147**, 100.
43. S. Varghese, M. G. Cutrufello, E. Rombi, C. Cannas, R. Monaci and I. Ferino, *Appl. Catal. A: Gen.*, 2012, **443-444**, 161.
44. X. Mo, Y.-T. Tsai, J. Gao, D. Mao and J. G. Goodwin, *J. Catal.*, 2012, **285**, 208.
45. S. Li, H. Wang, W. Li, X. Wu, W. Tang and Y. Chen, *Appl. Catal. B: Environ.*, 2015, **166-167**, 260.
46. M. Ding, J. Liu, Q. Zhang, N. Tsubaki, T. Wang and L. Ma, *Catal. Commun.*, 2012, **28**, 138.
47. Y. Lu, B. Cao, F. Yu, J. Liu, Z. Bao and J. Gao, *ChemCatChem*, 2014, **6**, 473.
48. C. N. Ávila-Neto, D. Zanchet, C. E. Hori, R. U. Ribeiro and J. M. C. Bueno, *J. Catal.*, 2013, **307**, 222.
49. Y. Xiang, R. Barbosa and N. Kruse, *ACS Catal.*, 2014, **4**, 2792.
50. N. Tien-Thao, M. Hassan Zahedi-Niaki, H. Alamdari and S. Kaliaguine, *J. Catal.*, 2007, **245**, 348.
51. V. Mahdavi, M. H. Peyrovi, M. Islami and J. Y. Mehr, *Appl. Catal. A: Gen.*, 2005, **281**, 259.

